Results from Automated Ionospheric Data Analysis for Ground-Based Augmentation Systems (GBAS)

Jiyun Lee*
Tetra Tech AMT
Sungwook Jung and Minchan Kim
*Korea Advanced Institute of Science and Technology**
and
Jiwon Seo, Sam Pullen, and Sigrid Close
Stanford University

ABSTRACT

Extremely large ionospheric spatial gradients could cause potential integrity threats to Ground-Based Augmentation System (GBAS) users. The importance of understanding ionosphere behavior is not limited to cases of extreme ionospheric events. Broader knowledge of both nominal and anomalous ionospheric behavior would help improve the design and operation of GBAS. We developed an automated tool for long-term ionosphere monitoring to continuously monitor ionospheric behavior during the life cycle of GBAS. This paper presents the results obtained from processing ionospheric data using the automated tool. Pre-existing ionospheric storm data are processed to populate the current threat space with newly discovered ionospheric anomalies. Durations of ionospheric anomalies exceeding a threshold within a continuous arc are also investigated in this research. This tool also supplies broader statistical estimates of ionospheric behavior under all conditions. In this paper, we analyze day-to-day variations of typical ionospheric statistics observed from a dense GPS network. The results demonstrate that some correlation between the statistics and a geomagnetic index exists even on nominal days. The automated tool not only identifies gradients large enough to threaten GBAS users but also provides reliable ionospheric statistics.

1.0. INTRODUCTION

Ground-Based Augmentation System (GBAS), such as Local Area Augmentation System (LAAS) developed by U.S. Federal Aviation Administration (FAA), supports an aircraft precision approach and landing by providing differential corrections and integrity information to aviation users. Because the distance between GBAS reference stations and users is less than several tens of kilometers and corrections are broadcasted twice in one second, differential errors due to spatial and temporal variation are almost negligible [1]. During the last peak of solar cycle, extreme ionospheric gradients of as large as 413 mm/km in the slant ionospheric delay domain were observed from the networks of the U.S. Wide Area Augmentation System (WAAS) and the Continuously Operating Reference Station (CORS) [2], [3]. If such gradients are not detected by the LAAS ground facility (LGF), users can suffer from correction errors of as large as 8 meters at the 200-foot decision height (DH) for a CAT I approach. The LAAS configuration, which is comprised of the LGF, aircraft, an ionospheric wave-front, and a Global Positioning System (GPS) satellite, is shown in Figure 1. The discovery of those extreme ionospheric gradients required the development of an ionospheric anomaly threat model for the LAAS operation. The model was used to simulate worst-case ionospheric errors that LAAS users might suffer and to develop mitigation strategies [3], [4], [5].

The current ionospheric threat model for LAAS in the Conterminous U.S. (CONUS) was derived from observation data on the network of CORS and WAAS reference stations. Figure 1 illustrates the parameters (slope, width, and speed of ionospheric wave-front) for the threat model with an assumption of a spatially linear semi-infinite wedge of constant speed motion. However, some uncertainty and limitations remain in the current threat model because it was constructed based upon a small number of severe ionospheric events during the last solar maximum period since 2000. Therefore, the threat model derived from past data should be validated during system operation by monitoring ionospheric behavior continuously and updating if necessary. In addition, receiver separations within the CORS network in CONUS

were typically 40 – 100 kilometers in the early 2000s, and these separations do not reflect the GBAS architecture. This study processes data collected recently from today's denser CORS network (over 1800 stations as of 2011) to observe ionospheric gradient estimates over separations of 10 – 40 km.

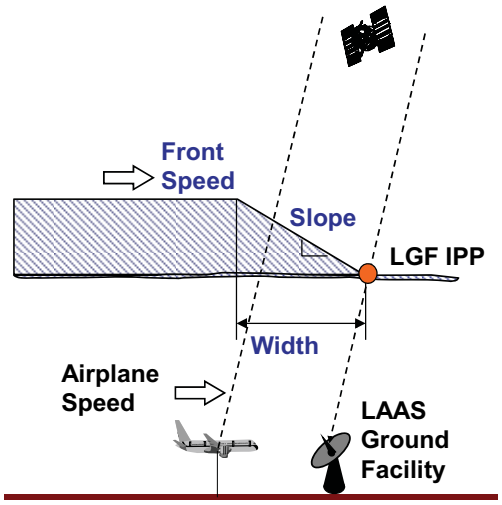

Figure 1. Illustration of a LAAS user impacted by an ionospheric wave-front (modeled as a linear semi-infinite wedge with the slope of the ramp, its width, and constant propagation speed).

An automated procedure for long-term ionosphere monitoring is needed to continually monitor ionosphere behavior over the operation period of GBAS as long as GBAS is dependent on the outer bounds of ionospheric threat models**.** In a previous study, we developed an automated Long-Term Ionospheric Anomaly Monitoring (LTIAM) tool and demonstrated that the tool can identifies extreme ionospheric anomalies that potentially violate the current threat model if any [6]. If extremely large gradients hazardous to GBAS users are identified, a procedure for manual validation should be triggered. In this research, the manual validation procedures were partially automated to simplify and systematize the remaining procedure. This further automation helps to limit the number of "false" gradients passed on to the manual validation procedure and to maximize utility of the LTIAM. The importance of understanding ionosphere behavior is not limited to cases of extreme ionospheric events. Comprehensive knowledge of both nominal and anomalous ionospheric behavior would help improve the design and operation of GBAS. The automated tool for the LTIAM also supplies reliable ionospheric gradient statistics under all conditions [7]. This paper presents more statistical results from a dense CORS network that has been expanded rapidly (over 1800 stations as of 2011) over the last decade. This study processes recently collected data to observe ionospheric gradient estimates over short baseline distances.

Section 2 introduces the dual-frequency GPS data and the geomagnetic indices used in this work. In Section 3, the basic algorithms and the upgraded algorithm of the LTIAM tool are reviewed and described. Monitoring results from case studies for ionospheric storm days and nominal days are presented in Section 4 and Section 5, respectively. This study is concluded in Section 6.

2.0. DATA

High-quality ionospheric measurements are required for long-term ionosphere monitoring. Ionospheric delays on GPS signals can be estimated precisely using dual-frequency observation data and sophisticated post-processing algorithms. The current ionospheric threat model for LAAS was derived from precise ionospheric delay estimates produced by Jet Propulsion Laboratory (JPL). Data collected from stations of the CORS and WAAS networks were post-processed by the "Supertruth" algorithm [8]. In the previous study, we developed and enhanced the "simple Truth" method, which is simpler and faster than the "Supertruth" algorithm [6], [7].

Table 1. Dates analyzed to develop the current ionospheric threat model.

Day (UT mm/dd/yy)	Kp	Dst
04/06/00	8.3	-287
04/07/00	8.7	-288
07/15/00	9.0	-289
07/16/00	7.7	-301
09/07/02	7.3	-177
10/29/03	9.0	-350
10/30/03	9.0	-383
10/31/03	8.3	-307
11/20/03	8.7	-422
07/17/04	6.0	-76

Table 2. Dates investigated to study day-to-day variations of typical ionospheric gradient statistics under nominal conditions.

Day (UT mm/dd/yy)	Kp	Dst
09/30/10	0.7	-11
10/01/10	0.7	-6
10/02/10	0.0	-6
10/03/10	1.0	-3
10/04/10	1.0	11
10/05/10	2.3	-15
10/06/10	2.3	-22

The dates from which data were collected and analyzed to evaluate the performance of the LTIAM tool are shown in Table 1 and Table 2. The geomagnetic conditions on these dates are shown with two indices of global geomagnetic activity from space weather databases: planetary K (Kp)

and *disturbance, storm time* (Dst). Kp represents solar particle effects on the Earth's magnetic fields, and is a three-hour composite index measured at several mid-latitude stations primarily located in the northern hemisphere [9], [10]. The Kp index ranges from 0 (no activity) to 9 (extreme activity) in thirds of an index unit. The Dst index measures equatorial magnetic disturbance derived from hourly scaling of low latitude horizontal magnetic variation [11], [12]. A negative Dst with a higher magnitude indicates that a more intense magnetic storm is in progress.

The dates shown in Table 1 are processed to populate the current Category-I (CAT-I) LAAS threat space with more ionospheric anomalies using the automated algorithms. These dates, on which ionospheric anomalies large enough to threaten LAAS users were discovered, were analyzed to develop the current threat model in the previous research [2], [3]. The maximum ionospheric gradient in slant domain was as large as 413 mm/km and observed on 20 November 2003 [2]. Table 2 shows the dates investigated to analyze day-to-day variations of typical ionospheric statistics. Seven consecutive days (one week) under quiet geomagnetic conditions were chosen for this analysis. The results of the ionospheric threat space population and the ionospheric statistics on the nominal days are presented in Sections 4.0 and Section 5.0, respectively.

3.0. AUTOMATED DATA PROCESS OF LTIAM

A methodology for the LTIAM was developed based on the data analysis and verification techniques used to generate the current threat model ([2], [3]) [6], [7]. The procedure consists of three steps as shown in Figure 2: Data Collection Processing (DCP), Ionospheric Anomaly Search Processor (IASP), and Reporting. Most of these steps are automated procedures, except the last step of IASP – Manual Validation (MV), which requires personal intervention – and Reporting. This section reviews each step presented in [6] and describes the new features of the LTIAM.

3.1. DATA COLLECTING PROSESSING

The automated tool for the LTIAM collects and processes two kinds of data (external data and GPS observation data) at a regular interval on a daily basis. DCP as a whole is composed of automated processes as shown in Figure 2. The external data are used to select potential periods and areas of anomalous ionospheric events and GPS observation data to estimate ionospheric delays and gradients so as to identify ionospheric anomalies.

In DCP, two indices of global geomagnetic activity from space weather databases: the Kp from the FTP server of National Oceanic and Atmospheric Administration (NOAA) [13], [14] and the Dst World Data Center for Geomagnetism at Kyoto University [15]. Additionally, the WAAS Grid Ionospheric Vertical Errors (GIVEs) at geographically fixed Ionospheric Grid Points (IGPs) [16] can be used to scan the ionospheric anomaly regions.

The GPS data of stations in the CORS network can be obtained from the CORS network FTP service [17], which allows access to anonymous users. The service provides GPS observation data, navigation data of GPS satellites, and coordinates of stations. The details of this service are described in [18].

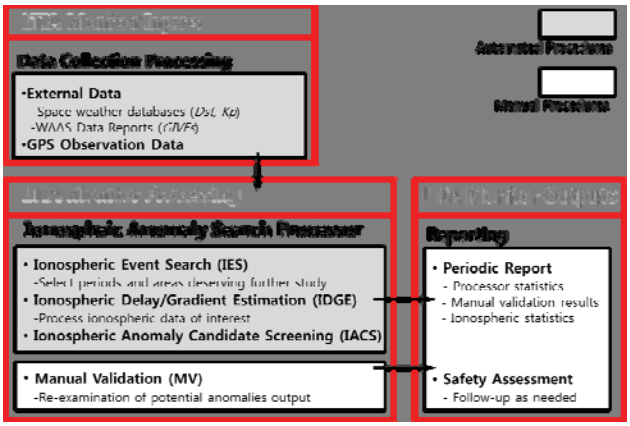

Figure 2. Methodology of automated Long-term Ionospheric Anomaly Monitoring (LTIAM).

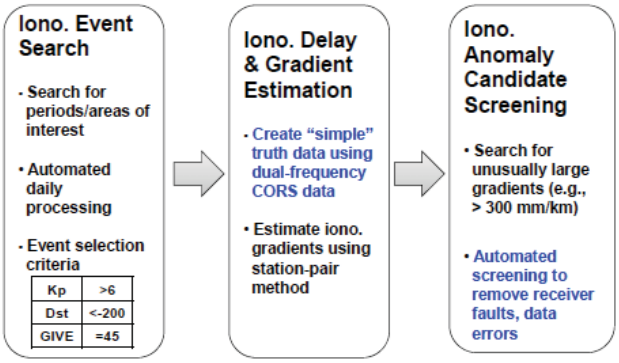

Figure 3. Automated procedures in Ionospheric Anomaly Search Processor.

3.2. IONOSPHERIC ANOMALY SEARCH PROCESSOR

The centerpiece of the automated LTIAM tool is IASP, which consists of Ionospheric Event Search (IES), Ionospheric Delay/Gradient Estimation (IDGE), Ionospheric Anomaly Candidate Screening (IACS), and Manual Validation (MV). As shown in Figure 2, the first three procedures are automated processes, and the last by manual. The specific procedures of the automated processes are described in Figure 3. In IASP, the data (described in Section 2.0) collected in the previous

procedure are processed to detect ionospheric anomalies on a daily basis.

An ionospheric anomalous day is evaluated with daily maximum values of the space weather indices by thresholds of 6 for Kp and -200 for Dst. Even when either of two criteria is satisfied, the requirement for ionospheric anomaly events is fulfilled.

Ionospheric gradients represent spatial decorrelation of ionosphere conditions between two GPS stations. Accuracy and precision of ionospheric gradients depend on an algorithm for the ionospheric delay estimation. Precise ionospheric delay estimates are generated from the "simple Truth" process that is simpler and faster than "Supertruth" process. Figure 4 shows the algorithm for generating "simple Truth" data in this research.

The dual-frequency GPS observation data, which are automatically collected from the CORS network FTP server, are inputs to the truth process. The slant ionospheric delay on the L1 frequency is computed from the L1/L2 code and carrier phase observations: the code-derived, I_ρ, and the carrier-derived, I_ϕ, measurements. The dual-frequency carrier-derived measurement evolves into the "simple Truth" data, and the code-derived measurement is used during the pre-process phase.

The pre-process includes continuous arc division, cycle slip detection, outlier removal, and ambiguity fixing (leveling). The cycle slip detection is implemented on the continuous arc (data gaps between consecutive continuous arcs are greater than 3600 seconds) in time. In the next step of cycle slip detection, short arc removal, and merging two consecutive sub-arcs, outlier detection and removal are performed for each continuous arc (or sub-arc). The carrier-derived observable, I_ϕ, contains integer ambiguities from both L1 and L2 frequencies. To remove these ambiguities, I_ϕ is fitted to I_ρ, introducing a level parameter, L [8], [19]. The leveled carrier-derived estimates, $I_{\phi\_leveled}$, can be written as

$$I_{\phi\_leveled} = I_\phi + L = I + \frac{c}{\gamma - 1}(IFB + \tau_{gd}) \quad . \qquad (1)$$
$$\gamma = \frac{f_{L1}^2}{f_{L2}^2}$$

In Equation (1), the receiver and satellite hardware biases (IFB and τ_{gd}) must be removed to obtain ionospheric delay estimates, I. The parameter γ is the squared L1/L2 frequency ratio and c is the speed of light in a vacuum.

The hardware biases in Equation (1) are also known as inter-frequency biases (IFBs). Ma and Maruyama [19] introduced a simpler and faster method to estimate a single receiver bias under the condition that satellite biases are known. We follow this simple method using satellite biases provided by International GNSS Service (IGS). The IGS ionosphere product can be obtained from four Global Data Centers (GDCs) of IGS via anonymous FTP services [20], [21]. The underlying assumption of this method is that the variation of vertical ionospheric delays from all visible satellites becomes minimal when the IFBs are correctly removed. The leveled carrier-derived estimates, $I_{\phi\_leveled}$, in Equation (1) are converted to equivalent vertical delays via a geometric mapping function, and used as inputs to a receiver IFB search algorithm. The best estimate of each receiver IFB is determined by searching for the one that minimizes the cumulative standard deviation of vertical ionospheric delays to their mean on a given day. An elevation cut-off angle of 30 degrees was applied for this algorithm to improve estimation accuracy.

After removing both receiver and satellite hardware biases from $I_{\phi\_leveled}$, we obtain precise ionospheric delay estimates, i.e., "simple Truth" data. Using this "simple Truth" solution and the well-known station pair method [2], the automated tool computes ionospheric gradients, ∇I , from all possible pairs of selected CORS stations looking at each satellite [6], [7].

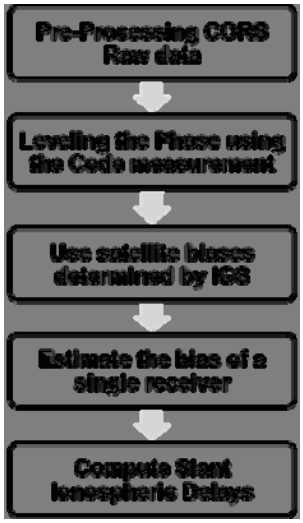

Figure 4. Algorithm for generating "simple Truth" data.

The automated process shown in Figure 3 searches severe ionospheric gradients, ∇I , that exceeds a threshold. Because a considerably large number of these gradients are not due to ionospheric events, an automated false-alarm screening process is added to eliminate those caused by any receiver faults or post-process errors. We added the new algorithm that uses the single frequency ionospheric estimates for the automated ionospheric anomaly screening. If a L1 code-minus-carrier measurement is not available at a given epoch where an extreme gradient is observed, the candidate is discarded because manual validation cannot be performed. In

addition, the candidate with a large discrepancy between the dual-frequency derived and the L1-only derived estimates is also discarded because those estimates are corrupted by receiver faults or post-processing errors. The new methods effectively discriminate misleading ionospheric anomaly candidates, and thus limit the number of "false" gradients passed on to manual validation.

More details for the automated algorithms are presented in our previous studies [6], [7].

Table 3. Monitoring result from case study on 20 Nov. 2003.

Procedure			Ionospheric Gradient (mm/km)	
			> 300	> 200
Total number of CORS stations in CONUS			368	
Number of stations with baseline ≤ 100 km			274	
Ionospheric anomaly Candidate screening (SV – Stn. pair)	Initial candidates		57	198
	Automated screening	Removed from negative delay check and excessive bias check	26	58
		Removed from L1 CMC check	6	31
Final ionospheric anomaly candidates			25	109
Manually validated anomalies			13	58

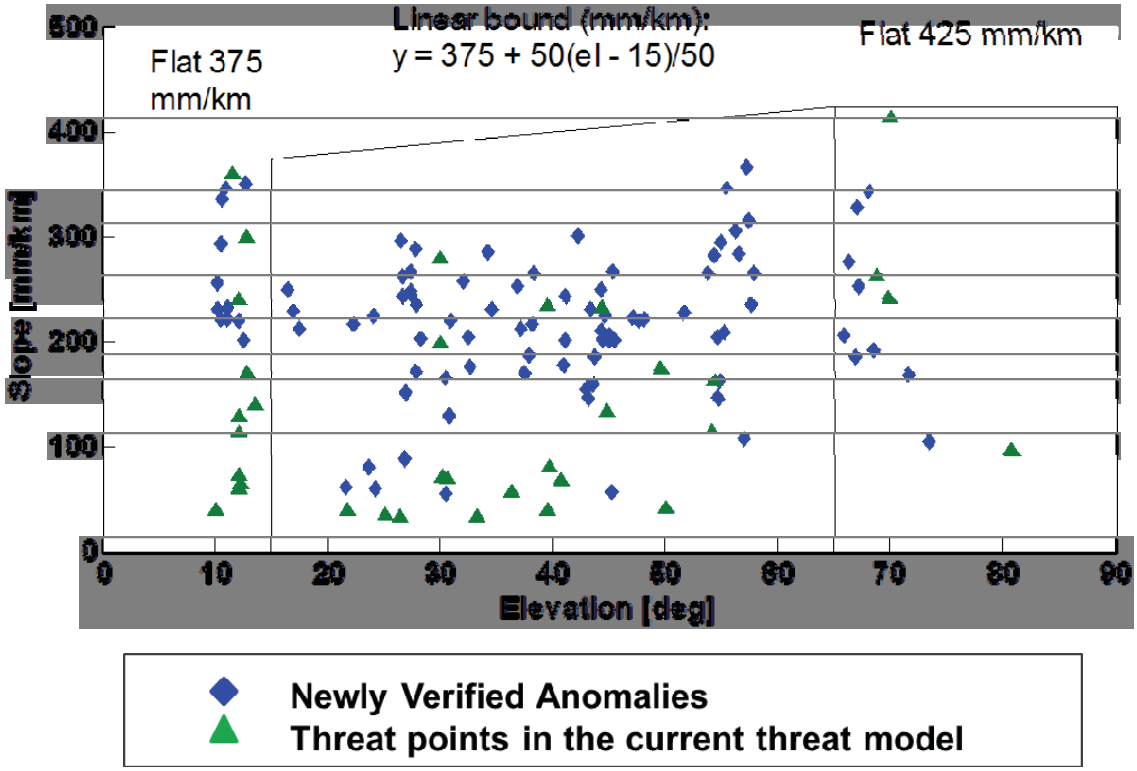

Figure 5. Ionospheric threat space with newly validated ionospheric anomalies.

4.0. MONITORING RESULTS: STORM DAYS

Using the automated LTIAM algorithms, the data on ionospheric storm days (shown in Table 1) investigated for the current threat model [2], [3] were processed to obtain results in storm conditions. The newly validated ionospheric anomalies were used to populate the current threat space.

4.1. CASE STUDY ON 20 NOVEMBER 2003

Among a total of 10 ionospheric storm days, the processor statistics on 20 Nov. 2003, which is the well-known ionospheric storm day, is shown in Table 3. Because the Kp index is greater than 6 and the Dst index is less than -200 as shown in Table 1, this date was automatically selected in the IES procedure. The total number of CORS receivers that have observation files is 368 in CONUS as of 20 Nov. 2003. Among these stations, the number of stations that have nearby stations within 100 km is 274. The automated algorithm collected GPS observation data of these stations and computed ionospheric gradients for all possible station pairs considering all satellites in view on both stations at the same epoch. With a lower threshold (200 mm/km) of the ionospheric gradients than that (300 mm/km) from the previous work [7], more ionospheric anomaly candidates were obtained after every procedure to screen the faulty ionospheric gradients. Among 198 initial candidates, 58 faulty candidates were removed from the original automated screening algorithms and further 31 candidates were screened out by the newly added L1-CMC automated check. All of the 109 remaining candidates went through the manual validation process, and those confirmed to be "true anomalies" were a total of 58 cases. We repeated this process for all ten ionospheric storm days and results are shown in the following subsection.

4.2. THREAT MODEL POPULATION

All of ten storm days listed in Table 1 were processed to populate the current threat space with more ionospheric anomalies. Figure 5 shows the ionospheric anomaly threat space with newly validated ionospheric anomalies discovered by the LTIAM tool. Green triangles (▲) present the threat points of the current threat model, and the threat points produced by the automated tool were added on the figure as blue diamonds (♦). In addition to the two maximum gradients (413mm/km at high elevation and 360 mm/km at low elevation) observed from early work [2], a total of 97 threat points were newly validated by the automated tool and the manual validation procedure. All these points are under the bound of the current threat model. The smaller threshold than 200 mm/km used in this study we choose or the more upcoming storm days we process, the more threat points should be discovered. These validated anomalies can be later used to estimate the rate of occurrence of anomalous events.

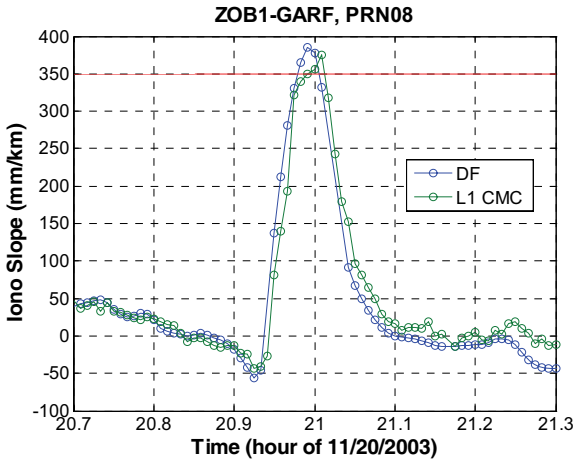

Figure 6. Maximum duration of extreme ionospheric gradient larger than 350 mm/km: dual-frequency (blue) and single-frequency (red) spatial gradient estimates between ZOB1 and GARF tracking PRN 08 at high elevation.

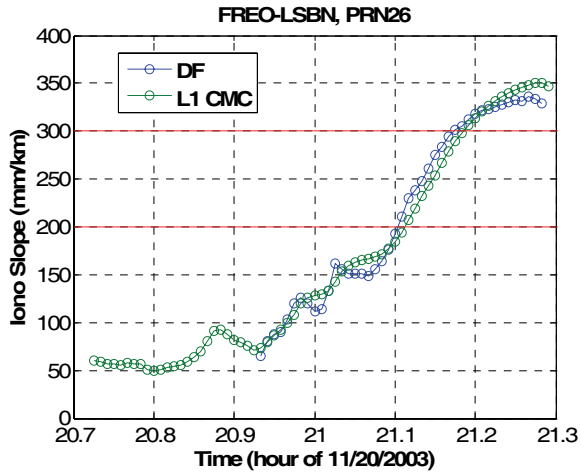

Figure 7. Maximum durations of extreme ionospheric gradients larger than 200 and 300 mm/km: dual-frequency (blue) and single-frequency (red) spatial gradient estimates between FREO and LSBN tracking PRN 26 at low elevation.

4.3. DURATION OF IONOSPHERIC ANOMALY

Durations of ionospheric anomalies exceeding a threshold within a continuous arc were also recorded. A total of 13 threat points whose gradients exceeded 300 mm/km were examined. Because erratic variations of ionospheric delay during extreme ionospheric activities could be detected as outliers on the ionospheric estimate process, a data outage could exist near the extreme gradient. Thus, raw (non-preprocessed) dual-frequency measurements of the ionospheric delay were used to estimate durations of ionospheric anomalies. If so many data outages of the

dual-frequency measurement existed on intervals of interest, the L1-only ionospheric estimate was used to compensate for the data outage of the dual-frequency observations.

The longest durations in which gradients of 200, 300, and 350 mm/km were exceeded were 649, 397, and 155 seconds, respectively. Figure 6 shows the ionospheric gradient of the dual-frequency and the L1 only estimates. The maximum duration of the ionospheric gradient greater than 350 mm/km was observed from this candidate. Figure 6 also shows the typical profile of the ionospheric gradient over time at a high elevation. The duration was estimated by measuring the time between two intersection points of the gradient curve and the horizontal line for the given gradient value. Figure 7 shows the ionospheric gradient profile that produced the longest durations of events with gradients greater than 200 and 300 mm/km. The profile represents the typical gradient at a low elevation, and the duration was measured from an intersection of the gradient curve and the threshold line to the endpoint of the measurement.

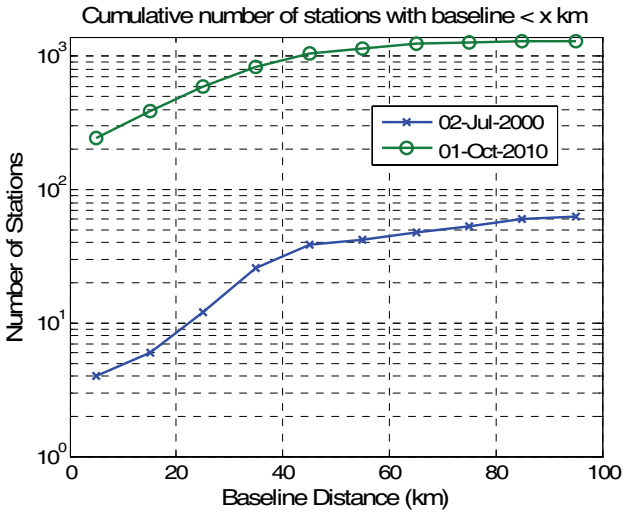

Figure 8. Cumulative numbers of CORS receivers in CONUS as a function of baseline distance between stations on 2 July 2000 and 1 October 2010.

5.0. STATISTICAL RESULTS: NOMINAL DAYS

To obtain statistical results on nominal days, seven case studies were conducted on the dates shown in Table 2. The geomagnetic activities on those seven days were quiet as shown from the geomagnetic indices in Table 2.

5.1. CORS NETWORK GROWTH

The CORS network has expanded since the early 2000s and thus the number of ground stations in CONUS has increased rapidly. Figure 8 shows a comparison of the CORS distributions in CONUS on 2 July 2000 and 1 October 2010. On these two days, the total numbers of stations in CONUS were 164 and 1371, respectively. The receiver separations within the CORS network prior to 2004 were typically 40 – 100 km or more as shown in Figure 8. Those did not reflect the GBAS architecture given that the distance between the LGF and users at the CAT I decision height (DH) is no more than 5 – 10 km. Since the enormous expansion of the CORS network has resulted in the increase of stations with the baselines less than 40 km, the monitoring results from recent observation data present more reasonable statistics in the short baseline.

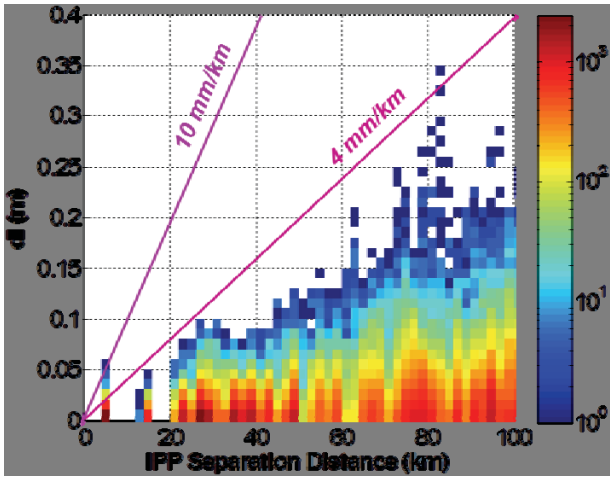

Figure 9. Differential vertical ionospheric delay results on a nominal day (2 July 2000) from JPL "Supertruth" data.

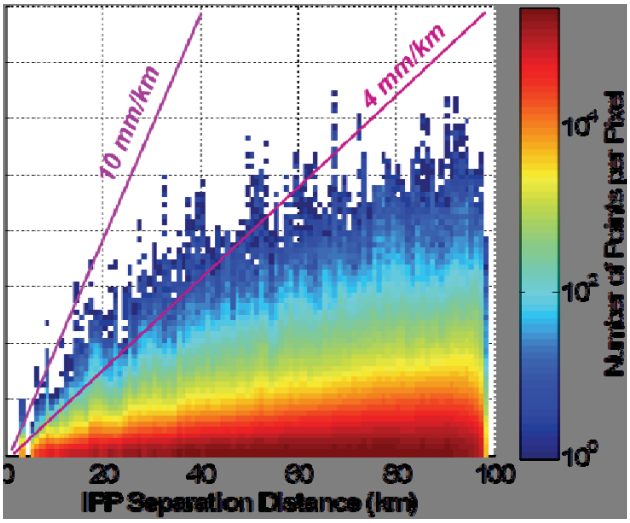

Figure 10. Differential vertical ionospheric delay results on a nominal day (1 October 2010) from "simple Truth" data.

5.2. STATISTICS OF IONOSPHERIC GRADIENTS

Excessive noise and bias errors in the "simple Truth" data should be removed to the extent possible to obtain reliable

statistics of ionospheric spatial gradients. To exclude noisy measurements due to multipath and receiver noise, we applied an elevation cutoff angle of 30 degrees. To remove remaining biases including the leveling error of dual-frequency carrier measurements and the inter-frequency bias (IFB) calibration error, we leveled differential ionospheric delays by subtracting off the mean of the differential ionospheric delays of continuous arcs. The continuous arcs were determined by applying the slip detection parameters of 5 – 10 cm depending on IPP separation distances.

Figure 9 and Figure 10 show the ionospheric spatial decorrelation results for two nominal days, 2 July 2000 and 1 October 2010, respectively. The horizontal axis divides the IPP separation distances into bins, and the vertical axis divides the differential vertical ionospheric delays into bins. The color of each bin presents the number of measurements counted. The differential delays were divided by the corresponding IPP distances to compute vertical ionospheric gradients.

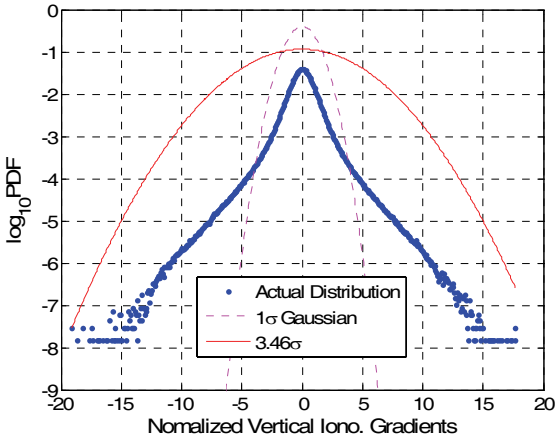

Figure 11. Probability density function of normalized vertical ionospheric gradients on a nominal day (1 October 2010).

In the case of 2 July 2000 (a well-known nominal day investigated in the previous work [1]), the data shortage exists in the short IPP separation distance range because of the low number density of stations in the early 2000s, as shown in Figure 9. The level of geomagnetic activity on this day was quiet (Kp of 1.7 and Dst of 2), and almost all measurements fall below 4 mm/km. It is noteworthy that 4 mm/km is the standard broadcast one-sigma value that was chosen as a conservative bound on nominal vertical ionospheric spatial gradients [1]. Figure 10 shows the spatial decorrelation result for a nominal day (1 October 2010) of seven days listed in Table 2. A large number of samples obtained from the dense CORS network and the "simple Truth" data can supply reliable ionospheric gradient statistics in the region below 40 km. It is also evident from the smoother linear behavior of differential ionospheric delays as a function of IPP separation than that shown in Figure 10.

The distribution of normalized vertical ionospheric gradients is shown in Figure 11 on a logarithmic scale. The vertical gradients were normalized by removing their mean and dividing them by their standard deviation. The actual distribution shown in Figure 11 has non-Gaussian tails. Because GBAS users assume a zero-mean normally distributed error model in the computation of protection levels, the nominal sigma (1σ) of a zero-mean Gaussian distribution (the dashed curve shown in Figure 11) should be inflated to cover the non-Gaussian tails of the actual distribution. The inflation factor, f, required for the data on 1 October 2010 was 3.46.

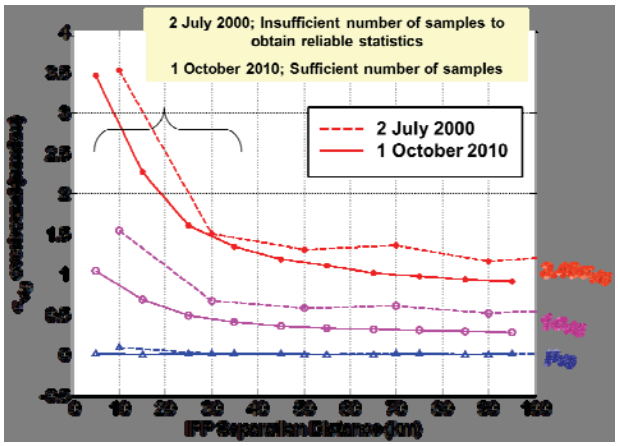

Figure 12. σ_{vig} overbound results for two nominal days: 2 July 2000 (from "simple Truth" data) and 1 October 2010 (from JPL "Supertruth" data).

To determine "σ_{vig} overbound", first vertical ionospheric gradients are divided into bins of IPP distance. Second, we compute the mean (μ_{vig}) and standard deviation (σ_{vig}) of vertical ionospheric gradients in each bin, and use these to normalize the gradients. Lastly, the "σ_{vig} overbound" is computed as $|\mu_{vig}| + f\,\sigma_{vig}$ for each bin. Figure 12 shows the σ_{vig} overbound results for two nominal days: 2 July 2000 from JPL "Supertruth" data and 1 October 2010 from "simple Truth" data. The curves with blue triangles, pink circles, and red circles present the means, the one-sigma values, and the σ_{vig} overbounds, respectively. The dashed line and the solid line show the results for 2 July 2000 and 1 October 2010, respectively. The estimates for 2 July 2000 at the IPP separation less than 40 km cannot be reliable because of the insufficient number of samples. The result from the recent observations shows a smoother curve of the σ_{vig} overbound than the result for the early 2000s because of the growth of the CORS network and the consequential enhancement in observation. Although an inversely proportional trend is observed due to the effect of remaining biases, the number of samples is sufficient to provide reliable statistics over the 10 – 40 km region.

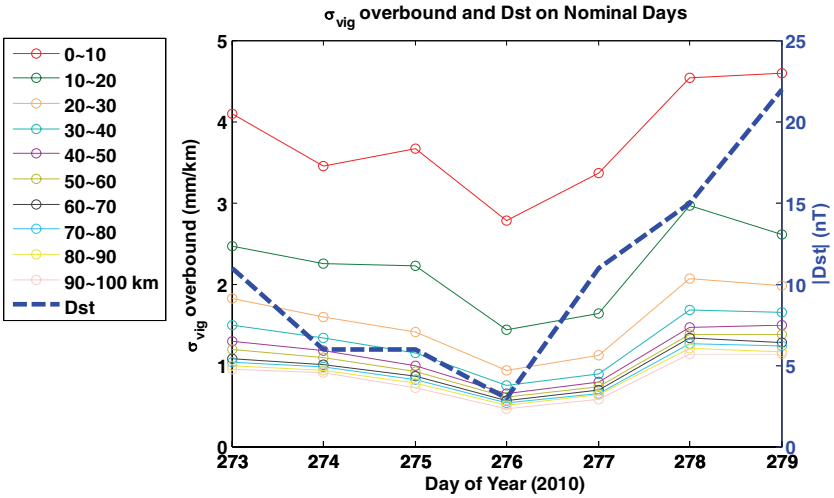

Figure 13. Day-to-day variations of ionospheric statistics on nominal days.

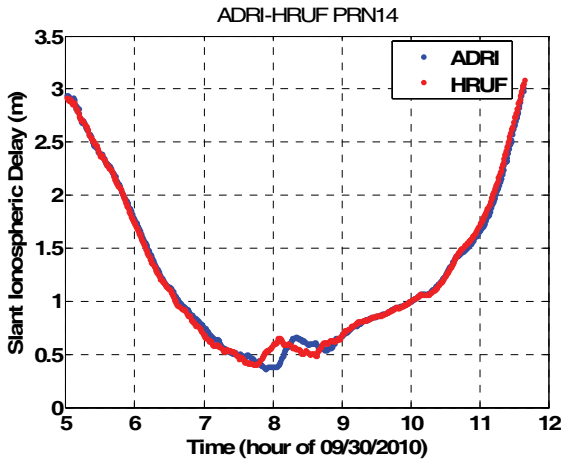

Figure 14. Small ionospheric disturbance under nominal condition: dual-frequency ionospheric delay estimates ("simple Truth" data) for receivers ADRI and HRUF tracking PRN 14.

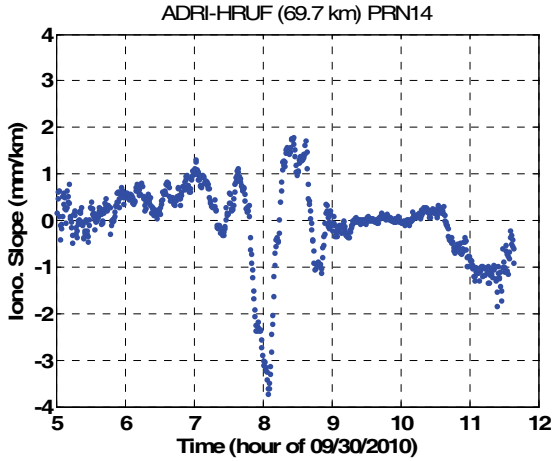

Figure 15. Spatial decorrelation of ionospheric delay ("simple Truth" data) under small ionospheric disturbance between receivers ADRI and HRUF tracking PRN 14.

5.3. DAY-TO-DAY VARIATIONS OF STATISTICS

Figure 13 shows the day-to-day variations of the ionospheric statistics over a week shown in Table 2. The first day on the horizontal axis in the figure (273 day of year 2010) corresponds to 30 September 2010. The curves with circles show the day-to-day variations of the typical ionospheric statistics at each IPP separation bin indicated by different colors. As shown in Figure 12, the remaining inter-frequency biases corrupt the ionospheric delay estimates. The effect of these biases is magnified when divided by the short baseline distances in the gradient domain. The blue dashed curve shows the variation of the Dst index. It is interesting to note that some correlation between the σ_{vig} overbound and the Dst index is observed even on nominal days. Although the variation of Dst is small under nominal conditions, it shows a similar pattern with that of σ_{vig}. Further investigation on the relationship between external ionospheric information (e.g., values of Kp, Dst, and WAAS GIVE) and observed gradients would be useful to utilize the LTIAM tool in a full range of ionospheric conditions.

Figure 14 shows a small disturbance of the ionosphere under nominal condition. The lay path of GPS signal of the station HRUF was first affected and then the station ADRI as the second by this disturbance. It produced a slant ionospheric gradient as large as 4 mm/km as shown in Figure 15. Knowing that the broadcast σ_{vig} of 4mm/km is a conservative bound on the gradient at the one-sigma level (i.e., not an upper bound), the probability of being greater than 4 mm/km would be approximately 0.32. Thus, the gradients ranged between 4 and 10 mm/km shown in Figure 10 is not abnormal, although the geomagnetic activity on this day was quiet (Kp of 0.7 and Dst of -6). In the analysis on nominal days, far fewer than 32% of the gradients are greater 4 mm/km.

6.0. CONCLUSION

This paper presents the results of the automated ionospheric data analysis to continuously monitor ionospheric events and check the validity of the current threat model over the life cycle of GBAS. The automation process is essential for the long-term ionosphere monitoring. The automation tool populated the current threat space with more ionospheric anomalies by processing the pre-existing ionospheric storm data. This result support that the use of the automated tool is sufficient to identify extreme ionospheric anomalies that may challenge the current threat model and to evaluate the validity of the model over the life cycle of the system. From the "simple Truth" data, the occurrence of the severe ionospheric event can be further estimated, and thus the broader understanding of the ionospheric anomalies is possible.

The results from the analysis of data under nominal conditions enable us to understand the typical ionospheric behavior. The permanent operation of the automated tool will categorize the ionospheric behavior in more detail for both nominal and anomalous conditions by producing the statistical results. If the pre-screening algorithm, by which the stations processed are pre-selected, is added to the automated tool, the data processing time can be saved by removing low-quality observation data. The continuous process and analysis using the automated tool will improve the GBAS design with enhanced integrity and availability. Consequently, this should also benefit future GBAS operations as well as global GBAS operations.

ACKNOWLEDGMENTS

The authors thank John Warburton of the FAA William J. Hughes Technical Center and his team for their support. We also would like to thank Jason Burns of the FAA, Oliver Jeannot, Cedric Lewis, Dieter Guenter, and Achanta Raghavendra of the AMT Tetra Tech, Attila Komjathy of the Jet Propulsion Laboratory, and Per Enge, Todd Walter, and Juan Blanch of Stanford for their support of this work. Jiwon Seo and Sigrid Close acknowledge the support of the National Science Foundation (AGS 1025262-002) and the Office of Naval Research (N00014-10-1-0450).

REFERENCES

[1] Lee, J, Pullen, S, Datta-Barua, S, and Enge, P, "Assessment of Ionosphere Spatial Decorrelation for Global Positioning System-Based Aircraft Landing System," AIAA *Journal of Aircraft*, Vol. 44, No. 5, 2007, pp. 1662-1669.

[2] Datta-Barua, S., Lee, J., Pullen, S., Luo, M., Ene, A., Qiu, D., Zhang G., and Enge, P., "Ionospheric Threat Parameterization for Local Area GPS-Based Aircraft Landing Systems," AIAA *Journal of Aircraft*, Vol. 47, No. 4, 2010, pp. 1141-1151.

[3] Lee, J., Datta-Barua, S., Zhang, G., Pullen, S., and Enge, P., "Observations of Low-Elevation Ionospheric Anomalies for Ground-Based Augmentation of GNSS,' *Radio Science*, Vol. 46, 2011, RS6005.

[4] Lee, J., Seo, J., Park, Y. S., Pullen, S., and Enge, P., "Ionospheric Threat Mitigation by Geometry Screening in Ground-Based Augmentation Systems," AIAA *Journal of Aircraft*, Vol. 48, No. 4, 2011, pp. 1422-1433.

[5] Seo, J., Lee, J., Pullen, S., Enge, P., and Close, S., "Targeted Parameter Inflation within Ground-Based Augmentation Systems to Minimize Anomalous Ionospheric Impact," AIAA *Journal of Aircraft*, in press.

[6] Lee, J., Jung, S., Bang, E., Pullen, S., and Enge, P., "Long Term Monitoring of Ionospheric Anomalies to Support the Local Area Augmentation System," *Proceedings of ION GNSS 2010*, Portland, OR, Sept. 21-24, 2010, pp. 2651-2660.

[7] Lee, J., Jung, S., and Pullen, S., "Enhancements of Long Term Ionospheric Anomaly Monitoring for the Ground-Based Augmentation System," *Proceedings of ION ITM 2011*, San Diego, CA, Jan. 24-26, 2011, pp. 930-941.

[8] Komjathy, A., Sparks, L, and Mannucci, A. J., "A New Algorithm for Generating High Precision Ionospheric Ground-Truth Measurements for FAA's Wide Area Augmentation System," Jet Propulsion Laboratory, JPL Supertruth Document, Vol. 1, Pasadena, LA, July 2004.

[9] Menvielle, M. and Berthelier, A., "The K-Derived Planetary Indices: Description and Availability," *Reviews of Geophysics*, Vol. 29, No. 3, 1991, pp. 415-432.

[10] Menvielle, M. and Berthelier, A., Correction to "The K-Derived Planetary Indices: Description and Availability," *Reviews of Geophysics*, Vol. 30, No. 1, 1992, p. 91.

[11] National Geophysical Data Center, "Space Physics Interactive Data Resource," 2005, http:/spidr.ngdc.noaa.gov/spidr/ [retrieved 1 March 2005].

[12] Sugiura, M. and Kamei, T., "Equatorial Dst Index 1957–1986," *International Association of Geomagnetism and Aeronomy*, Vol. 40, 1991, pp. 7–14.

[13] National Geophysical Data Center (NGDC) in National Oceanic and Atmospheric Administration (NOAA), "NOAA/National Geophysical data Center (NGDC) FTP Service," ftp://ftp.ngdc.noaa.gov [retrieved 25 May 2010].

[14] Space Weather Prediction Center (SWPC) in

National Oceanic and Atmospheric Administration (NOAA), "Space Weather Prediction Center Anonymous FTP Service," ftp://ftp.swpc.noaa.gov [retrieved 25 May 2010].
[15] Kyoto University, "World Data Center for Geomagnetism, Kyoto," http://wdc.kugi.kyoto-u.ac.jp [retrieved 28 May 2010].
[16] FAA/William J. Hughes Technical Center, "NSTB/Wide-Area Augmentation System Test Team," http://www.nstb.tc.faa.gov [retrieved 5 April 2010].
[17] National Geodesy Survey (NGS) in National Oceanic and Atmospheric Administration (NOAA), "CORS FTP Service," ftp://www.ngdc.noaa.gov/cors [retrieved 12 Aug. 2010].
[18] National Geodesy Survey (NGS) in National Oceanic and Atmospheric Administration (NOAA), "CORS: Continuously Operating Reference Stations," http://www.ngs.noaa.gov/CORS/ [retrieved 12 Aug. 2010].
[19] Ma, G. and Maruyama, T., "Derivation of TEC and Estimation of Instrumental Biases from GEONET in Japan", *Annales Geophysicae*, Vol. 21, 2003, pp. 2083-2093.
[20] Hernández-Pajares, M., Juan, J. M., Sanz, J., Orus, R., Garcia-Rigo, A., Feltens, J., Komjathy, A., Schaer, S. C., and Krankowski, A., "The IGS VTEC Maps: A Reliable Source of Ionospheric Information Since 1988," *Journal of Geodesy*, Vol. 83, No. 3-4, 2009, pp. 263-275.
[21] International GNSS Service (IGS) Central Bureau, "International GNSS Service," http://igscb.jpl.nasa.gov [retrieved 29 Jan. 2011].